Minimizing Current in Inductive Power Transfer Systems With an Asymmetrical Factor for Misalignment Tolerance and Wide Load Range

Zirui Yao, *Student Member, IEEE*, Junjie Zhang, Shiying Luo, Zhongbao Luo, Shaoting Zheng, Guanxi Li, Zhuhaobo Zhang, *Student Member, IEEE*, Philip T. Krein, *Fellow, IEEE*, and Hao Ma, *Senior Member, IEEE*

***Abstract*—In inductive power transfer (IPT) systems, misalignment and wide load range can lead to high current and control complexity. This can affect the performance of high-power systems. In this article, a method to minimize converter and primary resonant circuit currents based on an asymmetrical factor is proposed to improve IPT system performance over wide misalignment and load ranges. The proposed asymmetrical factor incorporates two design variables: an asymmetrical voltage factor and an asymmetrical compensation factor. These help to minimize current from two perspectives. First, they tend to redistribute zeroes and poles for power versus frequency characteristics. The power characteristic can be asymmetrical and monotonic over the working switching frequency range. Second, the input impedance angle can become insensitive to coupling factor and to load by adjusting the frequency that corresponds to the minimum input impedance angle. The current increases by only 15% over a 2:1 coupling coefficient variation range at rated load. Analysis and design guidelines are presented for the proposed method. A 2.1-kW prototype has been prepared to verify the approach.**

***Index Terms*—Asymmetrical factor, constant voltage charging, frequency control, inductive power transfer (IPT) system, misalignment tolerance.**

Manuscript received September 7, 2020; revised December 2, 2020 and February 2, 2021; accepted February 12, 2021. Date of publication February 24, 2021; date of current version June 1, 2021. This work was supported in part by the National Nature Science Foundation of China under Grant 51577171 and in part by the Zhejiang University/University of Illinois at Urbana-Champaign Institute, and was led by Principal Supervisors P. T. Krein and H. Ma. Recommended for publication by Associate Editor M. Recommended for publication by Associate Editor M. Duffy. *(Corresponding author: Hao Ma.)*

Zirui Yao, Zhuhaobo Zhang, and Hao Ma are with the College of Electrical Engineering, Zhejiang University, Hangzhou 310027, China, and also with the Zhejiang University/University of Illinois at Urbana-Champaign Institute, Haining 314400, China (e-mail: 11810009@zju.edu.cn; zzhbpain@163.com; mahao@zju.edu.cn).

Junjie Zhang, Shiying Luo, Zhongbao Luo, Shaoting Zheng, and Guanxi Li are with the College of Electrical Engineering, Zhejiang University, Hangzhou 310027, China (e-mail: 1290606384@qq.com; luoshiying0318@qq.com; 3150105623@zju.edu.cn; 3150103536@zju.edu.cn; 270342773@qq.com).

Philip T. Krein is with the College of Electrical Engineering, Zhejiang University, Hangzhou 310027, China , and also with the Zhejiang University/University of Illinois at Urbana-Champaign Institute, Haining 314400, China, and also with the University of Illinois at Urbana-Champaign, Champaign, IL 61820 USA (e-mail: krein@illinois.edu).

Color versions of one or more of the figures in this article are available online at https://doi.org/10.1109/TPEL.2021.3061920.

Digital Object Identifier 10.1109/TPEL.2021.3061920

I. Introduction

INDUCTIVE power transfer (IPT) systems are appealing for electric vehicle (EV) charging since they are contactless [1]–[5]. IPT systems, ranging from watts to multiple kilowatts, are used in commercial applications that include mobile devices [6], biomedical devices [7], electric bicycles [8], and electric cars [9]–[11]. Power levels from tens of kilowatts to megawatts are of interest for electric trains [12], electric ferries [13], and for fast charging [14]–[16]. Switching frequency limits and broader power ratings issues have limited the development of high power IPT systems [17], [18].

To minimize converter and primary resonant circuit currents and reduce control complexity for IPT systems, a method based on an asymmetrical factor is proposed in this article. With this method, current can be minimized when wide misalignment and load ranges are experienced. The realization uses a single IPT stage without extra hardware. This arrangement will be useful as power levels scale up. The method can ensure zero voltage switching (ZVS) over the allowed range of operating conditions. Based on analysis, the current increases by only 15% over a 2:1 coupling coefficient variation range at rated load.

High misalignment range and the need to support a wide load range are important factors in IPT converter and resonant circuit design. Currently, there are four key design considerations to achieve misalignment tolerance over a wide load range.

1) design of loosely coupled transformers;
2) compensation topologies;
3) converter control strategies;
4) variable inductor or capacitor methods.

In practice, multiple design considerations are combined for these purposes.

In prior work, loosely coupled transformers are usually designed to optimize misalignment tolerance. In [19]–[22], structures that include solenoidal arrangements [19], double D magnetics [20], double-D quadrature configurations [20], quadrature coils [21], and bipolar configurations [22] have been proposed to improve the misalignment range. An asymmetric coupling structure was presented in [23] based on concentrated magnetic flux. These structures can alleviate misalignment effects, but the coupling coefficient is low. In some methods, extra coils are added to improve output characteristics [24]–[26]. Although

primary current can be constant, added coils introduce extra losses, volume, and cost.

Known compensation topologies include fundamental structures, such as *LCC*, series-series (*S–S*), and series-parallel (*S–P*) circuits [27], [28]. In [29] and [30], multiple coupled coils support hybrid arrangements for compensation. Structures based on detuned conventional compensation topologies were proposed in [27] and [28] to maintain constant output characteristics with misalignment. The input impedance angle and primary current are proportional to the misalignment. Output characteristics can fluctuate between 10%–20%, and an extra dc-dc converter might be needed to regulate the output voltage for stable power transmission. In [29] and [30], hybrid structures were constructed with conventional series or parallel compensation circuits. Extra hardware results in extra losses and reduces system reliability, and the output power cannot be adjusted during the charging process. The output characteristics still fluctuate by about 5% within the optimized range of misalignment.

Pulse frequency modulation (PFM) [31], [32] and pulsewidth modulation (PWM) [34], [35] are used for converter control. When using PFM, frequency bifurcation can occur. This affects system stability [33]. In [32], a strategy to avoid frequency bifurcation was designed. Current is proportional to misalignment, and efficiency decreases as the load resistance or misalignment increase. When hard switching is employed for PWM converters, the impact can be reduced by employing a frequency control method [34] or by using wide-bandgap semiconductors [36]. The misalignment and load range are still limited by power device current ratings, since current is inversely proportional to duty ratio. In [35], a dual-side control strategy that integrates phase shift with active rectification is proposed to extend the misalignment and load range. In this method, extra switches and controllers are needed.

Methods with variable inductors [37] or capacitors [38]–[40] adjust output characteristics by introducing new control variables. In [37], the inductor value is adjusted to match conditions. With this method, current changes substantially with misalignment but less over a wide load range. A method for changing the equivalent capacitance of a capacitor matrix was proposed in [38] to provide impedance matching for a given misalignment. This method uses discrete steps. A switch-controlled capacitor is proposed in [39] and [40] to provide continuous adjustment with good system efficiency. In the arrangement, the resonant capacitor carries high current and voltage. Power device ratings and isolation problems limit the ability to scale this approach to higher power systems.

The asymmetrical factor introduced in this article builds on this prior work to address simultaneous challenges of wide misalignment range and wide load range. Converter and primary resonant circuit currents are held near their minimums across the target operating range.

In this article, the content is organized as follows. The analysis of a conventional symmetrical S-S compensation IPT system is described in Section II. The proposed asymmetrical factor method is analyzed for various scenarios in Section III. Design procedures are provided and system performance is evaluated for the proposed method in Section IV. Experimental results and comparisons with a symmetrical method are presented in Section V. Finally, conclusions is drawn in Section VI.

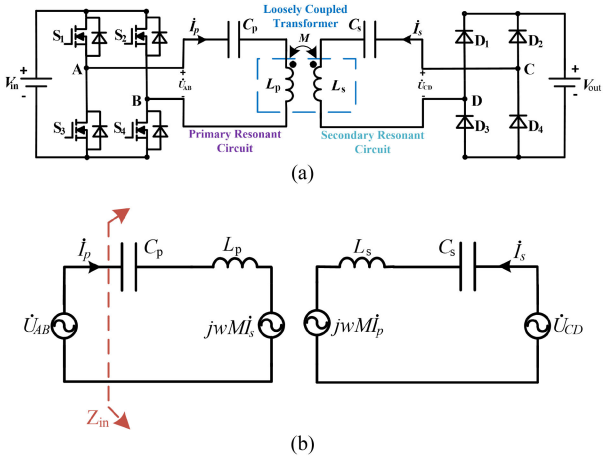

Fig. 1. S-S compensation IPT system. (a) *S–S* compensation topology. (b) Simplified equivalent circuit.

II. Analysis of a Conventional Symmetrical Series-Series Compensation IPT System

A general *S–S* compensation IPT system is shown in Fig. 1(a). The loosely coupled transformer includes primary coil $L_{\rm p}$ and secondary coil $L_{\rm s}$. A MOSFET bridge (S_1, S_2, S_3, S_4) drives the primary. The secondary resonant circuit transfers power to a load, modeled as a constant voltage $V_{\rm out}$, through a diode bridge (D_1, D_2, D_3, D_4).

The fundamental harmonic is used for analysis, consistent with resonant operation. The storage components are taken to be ideal for initial analysis. The simplified equivalent circuit is shown in Fig. 1(b). The effective values of first-harmonic voltages $U_{\rm AB}$ and $U_{\rm CD}$ are

$$U_{AB} = \frac{2\sqrt{2}}{\pi} V_{\rm in},\ U_{CD} = \frac{2\sqrt{2}}{\pi} V_{\rm out}. \tag{1}$$

Primary and secondary resonances are associated with frequencies

$$\omega_p = 2\pi f_p = \frac{1}{\sqrt{L_p C_p}},\quad \omega_s = 2\pi f_s = \frac{1}{\sqrt{L_s C_s}}. \tag{2}$$

For a given frequency ω to be considered, the coupled voltage relationships are

$$\begin{cases} \dot{U}_{AB} = (j\omega L_p - \frac{1}{j\omega C_p})\dot{I}_p + j\omega M \dot{I}_s \\ \dot{U}_{CD} = (j\omega L_s - \frac{1}{j\omega C_s})\dot{I}_s + j\omega M \dot{I}_p \\ M = k\sqrt{L_p L_s}, \end{cases} \tag{3}$$

where k is the transformer coupling coefficient. It is noted that $\dot{U}_{CD}$ and $\dot{I}_s$ are out of phase because of the rectifier bridge. Combining (2) and (3), the power transferred to the load P is

$$P = \frac{{U_{CD}}^2 \sqrt{\omega^2 \frac{k^2}{{\tau_u}^2} - \left(\omega - \frac{{\omega_p}^2}{\omega}\right)^2}}{L_s[\omega^2 k^2 - (\omega - \frac{{\omega_p}^2}{\omega})(\omega - \frac{{\omega_s}^2}{\omega})]} \tag{4}$$

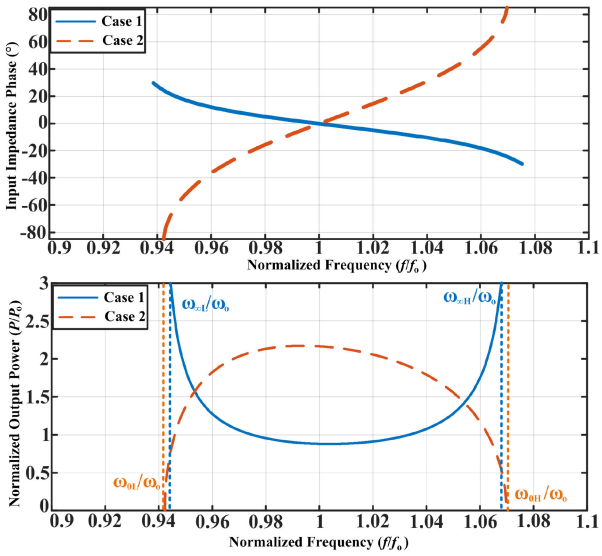

Fig. 2. Comparison between characteristics of the IPT system with case 1 and with case 2 when $\omega_p = \omega_s$.

where an asymmetrical voltage factor $\tau_{\rm u}$ has been defined as

$$\tau_u = \frac{U_{CD}}{U_{AB}}\sqrt{\frac{L_p}{L_s}}. \tag{5}$$

This adjusted voltage transfer ratio affects power vs. frequency characteristics [18], [41].

When both circuits are tuned to matched resonant frequency $\omega_{\rm o}$, (4) becomes

$$P = \frac{{U_{CD}}^2\sqrt{\omega^2\frac{k^2}{{\tau_u}^2} - \left(\omega - \frac{{\omega_o}^2}{\omega}\right)^2}}{L_s[\omega^2k^2 - \left(\omega - \frac{{\omega_o}^2}{\omega}\right)^2]}. \tag{6}$$

The input impedance angle can be obtained from (3)

$$\theta = \angle(Z_{\rm in}) = \arctan\left[\frac{(1-\frac{1}{{\tau_u}^2})(1-\frac{{\omega_o}^2}{\omega^2})}{\sqrt{\frac{k^2}{{\tau_u}^2} - \left(1-\frac{{\omega_o}^2}{\omega^2}\right)^2}}\right] \tag{7}$$

where θ is the angle between $\dot{U}_{AB}$ and $\dot{I}_p$, and $Z_{\rm in}$ is the equivalent input impedance shown in Fig. 1(b). Power characteristics and phase angle near the resonant frequency are shown in Fig. 2. It is convenient to define case 1, for which $\tau_u \le 1$, and case 2, with $\tau_u > 1$ [18]. The range from $\omega_{\infty\rm L}/\omega_{\rm o}$ to $\omega_{\infty\rm H}/\omega_{\rm o}$ is the working switching frequency range for case 1, and the range from $\omega_{0\rm L}/\omega_{\rm o}$ to $\omega_{0\rm H}/\omega_{\rm o}$ is the working switching frequency range for case 2. The various frequencies are defined below in detail in Section III-A.

As in Fig. 2, the frequency has been normalized to the matched resonant frequency $f_{\rm o}$. Case 1 yields a concave power function with a minimum value at the resonant frequency and the range from $\omega_{\infty\rm L}/\omega_{\rm o}$ to $f/f_{\rm o}$ or from $f/f_{\rm o}$ to $\omega_{\infty\rm H}/\omega_{\rm o}$ is selected to control the output power. Case 2 yields a convex power function with a maximum value at the resonant frequency and the range from $\omega_{0\rm L}/\omega_{\rm o}$ to $f/f_{\rm o}$ or from $f/f_{\rm o}$ to $\omega_{0\rm H}/\omega_{\rm o}$ is selected to control the output power. The power at the resonant frequency in case 1 needs to be 5%–10% of rated power to yield misalignment tolerance over a wide load range. This increases the mutual inductance and may decrease efficiency. Case 2 adapts well to a wide load range due to its convex power characteristic.

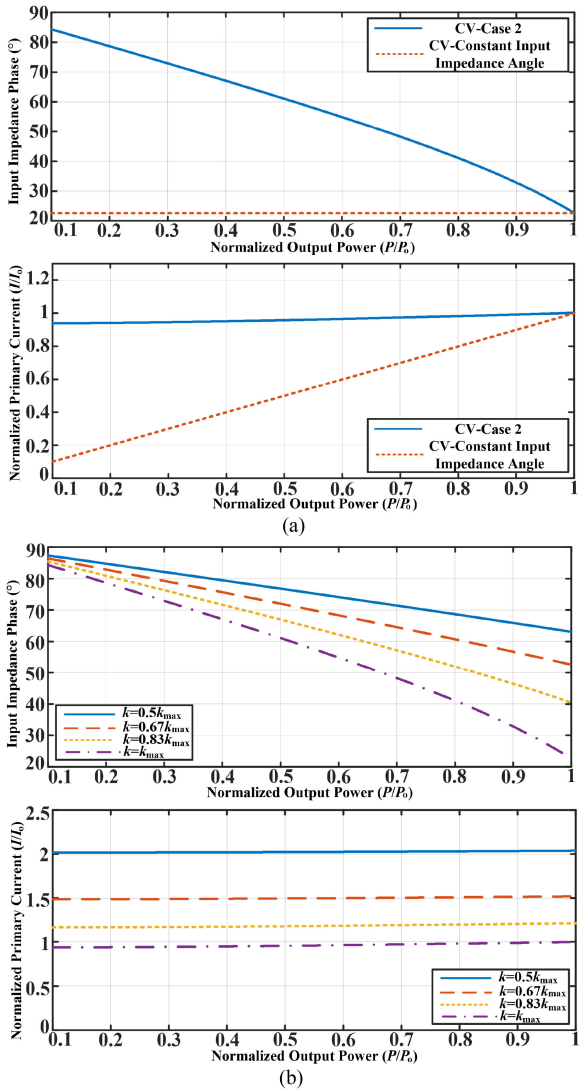

Fig. 3. Input impedance angle and primary current for case 2, and $k_{\rm max} = 0.31$. (a) Comparisons between case 2 and constant input impedance angle over a 10:1 load range at $k_{\rm max}$. (b) Results with case 2 over a 10:1 load range for various coupling coefficients.

Circuit analysis shows that converter apparent power is proportional to primary current because the input first-harmonic voltage is constant with PFM control. The primary current is affected by the input impedance angle. Thus, primary current or input impedance angle can serve as an optimization target for minimizing converter and primary resonant circuit currents.

In practice, in case 2, an inductive input impedance is expected to achieve ZVS by adjusting the switching frequency slightly higher than the resonant frequency. The input impedance angle and the primary current for case 2 over a 10:1 load range are shown in Fig. 3. Fig. 3(a) compares results between case 2 and constant input impedance angle at maximum coupling. Fig. 3(b) shows results with case 2 for various coupling values. As shown

in Fig. 3(a), in case 2 the input impedance angle increases as output power decreases. This will increase the primary current at light load. As illustrated in Fig. 3(b), the wider the coupling coefficient range, the larger the input impedance angle will be. At a given output power, a larger input impedance angle will result in higher primary current.

III. Analysis of the Proposed Asymmetrical Factor Method

As explained in Section II, the conventional symmetrical *S–S* compensation method cannot minimize current when wide misalignment and load ranges are experienced. Case 1 has better misalignment performance, but it cannot achieve a wide load range [18]. Case 2 can support misalignment and wide load ranges, but because of high input impedance angle, the primary current will increase with misalignment for a given load [32]. This will increase the input apparent power. In this section, a proposed asymmetrical method is analyzed, intended to alter this tradeoff and support lower current. The power characteristic and input impedance angle are optimized for better misalignment performance over a wide load range.

A. Analysis of Asymmetrical and Monotonic Power Characteristics

The zeroes and poles of (4) are

$$\begin{cases} {\omega_{0L}}^2 = \frac{{\omega_p}^2}{1+\frac{k}{\tau_u}} \\ {\omega_{0H}}^2 = \frac{{\omega_p}^2}{1-\frac{k}{\tau_u}} \\ {\omega_{\infty L}}^2 = \frac{{\omega_p}^2+{\omega_s}^2-\sqrt{({\omega_p}^2-{\omega_s}^2)^2+4k^2{\omega_p}^2{\omega_s}^2}}{2(1-k^2)} \\ {\omega_{\infty H}}^2 = \frac{{\omega_p}^2+{\omega_s}^2+\sqrt{({\omega_p}^2-{\omega_s}^2)^2+4k^2{\omega_p}^2{\omega_s}^2}}{2(1-k^2)} \end{cases} \tag{8}$$

where $\omega_{0\mathrm{L}}$, $\omega_{0\mathrm{H}}$ are the zeroes and $\omega_{\infty\mathrm{L}}$, $\omega_{\infty\mathrm{H}}$ are the poles. In practice, the range between zeroes and poles that contains the resonant frequencies is selected as working switching frequency range, as shown in Fig. 2.

In case 1, the zeroes and poles are distributed as $\omega_{0\mathrm{L}} < \omega_{\infty\mathrm{L}} < \omega_{\infty\mathrm{H}} < \omega_{0\mathrm{H}}$. In case 2, they follow $\omega_{\infty L} < \omega_{0L} < \omega_{0H} < \omega_{\infty H}$. In both cases, when primary and secondary resonant frequencies match, the zeroes and poles are distributed symmetrically around the resonant frequency. This also leads to a symmetrical distribution of power characteristics about $\omega = \omega_{\mathrm{o}}$.

An asymmetrical compensation factor τ_{c}

$$\tau_c = \frac{\omega_s}{\omega_p} \tag{9}$$

can be defined, and is non-unity when the primary and secondary frequencies do not match. Analogous to symmetrical conditions, asymmetrical conditions can also be divided into two cases. Frequency case 1 has $\omega_{0\mathrm{L}}<\omega_{\infty\mathrm{L}}<\omega_{0\mathrm{H}}<\omega_{\infty\mathrm{H}}$. The working switching frequency range is between $\omega_{\infty\mathrm{L}}$ and $\omega_{0\mathrm{H}}$. The constraints are

$$\frac{k}{1-\lambda} < \tau_u < \frac{k}{1+\lambda} \tag{10}$$

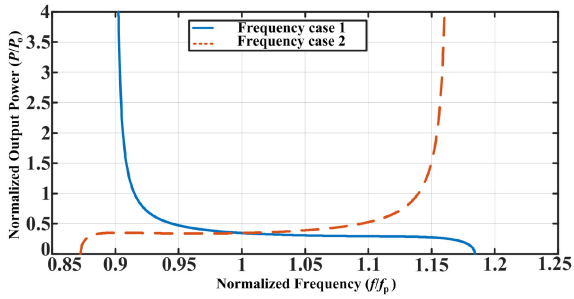

Fig. 4. Asymmetrical power profiles for frequency cases 1 and 2.

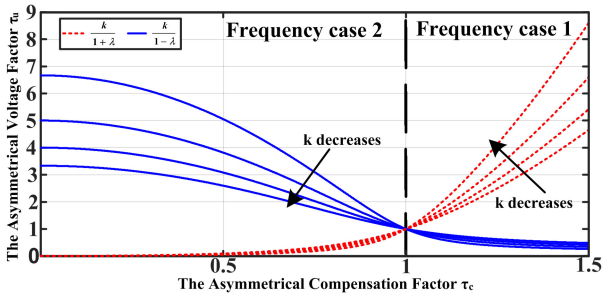

Fig. 5. Limiting values $k/(1+\lambda)$ and $k/(1-\lambda)$ as a function of the asymmetrical compensation factor τ_c.

where

$$\lambda = \frac{2(1-k^2)}{(1+{\tau_c}^2)+\sqrt{({\tau_c}^2-1)^2+4k^2{\tau_c}^2}}.$$

Frequency case 2 has $\omega_{\infty\mathrm{L}}<\omega_{0\mathrm{L}}<\omega_{\infty\mathrm{H}}<\omega_{0\mathrm{H}}$. The working switching frequency range is between $\omega_{0\mathrm{L}}$ and $\omega_{\infty\mathrm{H}}$. The constraints are

$$\frac{k}{1+\lambda} < \tau_u < \frac{k}{1-\lambda}. \tag{11}$$

The power characteristic is asymmetrical within the working switching frequency range, as shown in Fig. 4, where frequency has been normalized to primary resonance f_{p}.

Plots of the limiting values $k/(1+\lambda)$ and $k/(1-\lambda)$ in (10) and (11) are shown in Fig. 5 for asymmetrical voltage factor τ_u and asymmetrical compensation factor τ_{c}. In Frequency case 1, the asymmetrical voltage factor τ_{u} increases as the coupling coefficient decreases. This is reversed in Frequency case 2. If the derivative of (4) with respect to frequency fulfills

$$\begin{cases} \frac{\partial P}{\partial \omega} < 0 & (\omega_{\infty L} < \omega < \omega_{0H}) \text{ Frequency case 1} \\ \frac{\partial P}{\partial \omega} > 0 & (\omega_{0L} < \omega < \omega_{\infty H}) \text{ Frequency case 2} \end{cases} \tag{12}$$

the power characteristic will be monotonic within the working switching frequency range.

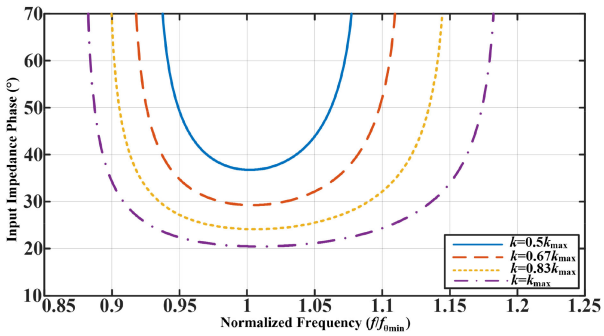

Fig. 6. Characteristics of input impedance angle for $k_{\max}=0.31$ and $\tau_c=1.05$ with various coupling coefficients, frequency case 1.

B. Analysis of the Asymmetrical Compensation Factor

If the primary and secondary resonances do not match, the input impedance angle becomes

$$\theta=\angle(Z_{in})=\arctan\left[\frac{(1-\frac{{\omega_p}^2}{\omega^2})-\frac{1}{{\tau_u}^2}(1-\frac{{\omega_s}^2}{\omega^2})}{\sqrt{\frac{k^2}{{\tau_u}^2}-(1-\frac{{\omega_p}^2}{\omega^2})^2}}\right]. \quad (13)$$

In frequency case 1 with $\tau_c>1$, the secondary resonant frequency f_s is higher than the primary resonant frequency f_p. The input impedance angle has the same sign as the numerator of the arctangent in (13), implying various cases for τ_u

$$\left(1-\frac{{\omega_p}^2}{\omega^2}\right)-\frac{1}{{\tau_u}^2}\left(1-\frac{{\omega_s}^2}{\omega^2}\right)>0$$
$$\Rightarrow\begin{cases}{\tau_u}^2<\frac{{\omega_s}^2-\omega^2}{{\omega_p}^2-\omega^2}={\tau_c}^2+\frac{({\tau_c}^2-1)\omega^2}{{\omega_p}^2-\omega^2} & (\omega\le\omega_p)\\ {\tau_u}^2>0>\frac{\omega^2-{\omega_s}^2}{\omega^2-{\omega_p}^2} & (\omega_p<\omega<\omega_s)\\ {\tau_u}^2>\frac{\omega^2-{\omega_s}^2}{\omega^2-{\omega_p}^2}=1+\frac{(1-{\tau_c}^2){\omega_p}^2}{\omega^2-{\omega_p}^2} & (\omega\ge\omega_s).\end{cases} \quad (14)$$

When $\omega_p<\omega<\omega_s$, the input impedance angle is positive. In frequency case 1, an inductive impedance should be selected.

In frequency case 2 with $\tau_c<1$, the primary resonant frequency f_p is higher than the secondary resonant frequency f_s. The numerator of the arctangent in (13) is now negative, and implies a different set of cases for τ_u

$$(1-\frac{{\omega_p}^2}{\omega^2})-\frac{1}{{\tau_u}^2}(1-\frac{{\omega_s}^2}{\omega^2})<0$$
$$\Rightarrow\begin{cases}{\tau_u}^2>\frac{{\omega_s}^2-\omega^2}{{\omega_p}^2-\omega^2}={\tau_c}^2+\frac{({\tau_c}^2-1)\omega^2}{{\omega_p}^2-\omega^2} & (\omega\le\omega_s)\\ {\tau_u}^2>0>\frac{\omega^2-{\omega_s}^2}{\omega^2-{\omega_p}^2} & (\omega_s<\omega<\omega_p)\\ {\tau_u}^2<\frac{\omega^2-{\omega_s}^2}{\omega^2-{\omega_p}^2}=1+\frac{(1-{\tau_c}^2){\omega_p}^2}{\omega^2-{\omega_p}^2} & (\omega\ge\omega_p).\end{cases} \quad (15)$$

When $\omega_s<\omega<\omega_p$, the input impedance angle is negative and a capacitive impedance should be selected.

Because ZVS in the primary inverter will improve system efficiency, an inductive input impedance is expected for wide misalignment and load ranges. Frequency case 1 is preferred on this basis. The characteristics of input impedance angle for various coupling coefficients are shown in Fig. 6. All of the angles are positive within a range of interest, and therefore the input acts as an inductive load.

As indicated in Fig. 6, the input impedance angle has a minimum value. In this figure the frequency has been normalized to frequency that corresponds to the minimum input impedance angle $f_{\theta\min}$. To improve misalignment tolerance, the minimum value should be selected to coincide with a frequency that is insensitive to coupling coefficient. System performance can be improved and current can be minimized by minimizing sensitivity of input impedance angles to coupling coefficient. When the coupling coefficient changes, the variation in input impedance angle is

$$\begin{cases}\frac{\tan\theta_{k\min}}{\tan\theta_{k\max}}=\frac{\sqrt{\frac{{k_{\max}}^2}{{\tau_u}^2}-(1-\frac{{\omega_p}^2}{\omega^2})^2}}{\sqrt{\frac{{k_{\min}}^2}{{\tau_u}^2}-(1-\frac{{\omega_p}^2}{\omega^2})^2}}=\sqrt{\alpha^2+\frac{(\alpha^2-1)(1-\frac{{\omega_p}^2}{\omega^2})^2}{\frac{{k_{\min}}^2}{{\tau_u}^2}-(1-\frac{{\omega_p}^2}{\omega^2})^2}}\\ k_{\max}=\alpha k_{\min}(\alpha>1)\end{cases} \quad (16)$$

where $\theta_{k\min}$ and $\theta_{k\max}$ are the angles corresponding to the minimum coupling coefficient $k_{\min}$ and the maximum coupling coefficient $k_{\max}$, respectively. From (16), when coupling changes, the minimum variation in input impedance angle occurs at $\omega=\omega_p$.

To ensure that the minimum input impedance angle coincides with $\omega=\omega_p$, the derivative of (13) with respect to frequency should be zero at $\omega=\omega_p$, so

$$\frac{\partial\theta}{\partial\omega}\Big|_{\omega=\omega_p}$$
$$=\frac{(1-\frac{{\tau_c}^2}{{\tau_u}^2})\kappa-[(1-\frac{1}{{\tau_u}^2})+(\frac{{\tau_c}^2}{{\tau_u}^2}-1)\frac{{\omega_p}^2}{\omega^2}](\frac{{\omega_p}^2}{\omega^2}-1)}{\left\{1+\frac{[(1-\frac{1}{{\tau_u}^2})+(\frac{{\tau_c}^2}{{\tau_u}^2}-1)\frac{{\omega_p}^2}{\omega^2}]^2}{\kappa}\right\}\kappa^{\frac{3}{2}}}=0$$
$$\Rightarrow(1-\frac{{\tau_c}^2}{{\tau_u}^2})\frac{k^2}{{\tau_u}^2}=0$$
$$\Rightarrow\tau_u=\tau_c \quad (17)$$

where

$$\kappa=\frac{k^2}{{\tau_u}^2}-\left(1-\frac{{\omega_p}^2}{\omega^2}\right)^2.$$

Therefore, to provide minimum input impedance angle at ω_p, the asymmetrical voltage factor τ_u should match the asymmetrical compensation factor τ_c. This choice also minimizes sensitivity of the input impedance angle to coupling, in turn providing consistent system performance over a wide misalignment range. Given this objective, the two factors can be treated together as a single "asymmetrical factor" τ.

IV. Design Procedure and System Performance

The IPT system specifications and the design target ranges in which the proposed method seeks to minimize current are given in Table I. The system allows a 10:1 load range, although minimization is sought over a 2:1 load range and 2:1 coupling range. In this section, design procedures are provided and system performance is evaluated based on the single asymmetrical factor τ.

TABLE I
SPECIFICATIONS OF THE IPT SYSTEM

Parameters	Values
Power rating	2.1 kW
Input voltage	315 V
Output voltage	300 V
Output current range	0.7-7 A
Design target coupling range	0.15-0.31
Nominal load range	43-430 Ω
Design target load range	$0.5P_o$- P_o

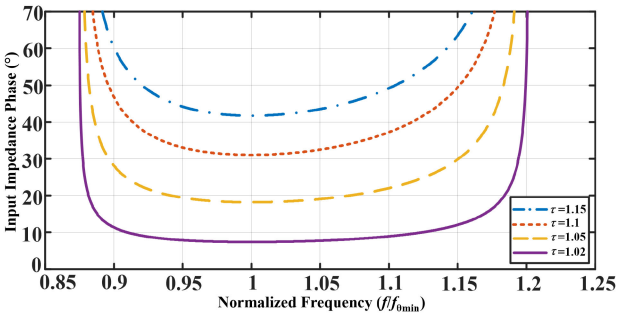

Fig. 7. Characteristics of input impedance angle for various asymmetrical factors at a given coupling coefficient $k = 0.31$.

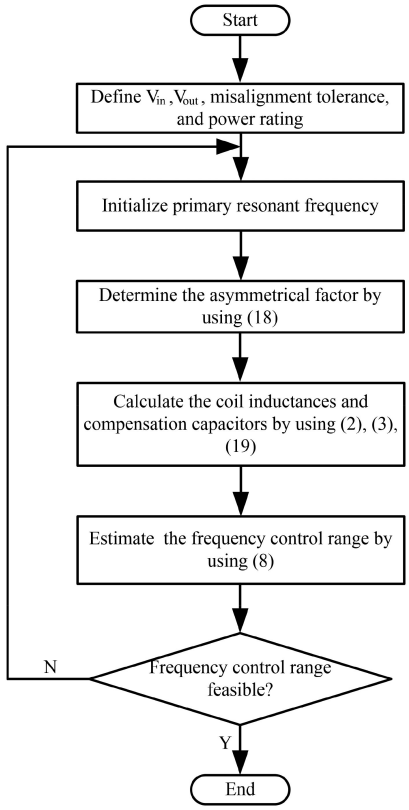

Fig. 8. Flowchart for design with the proposed method.

A. Applying the Asymmetrical Factor

Combining the analysis of the asymmetrical factor in Section III with ZVS operation, design constraints become

$$\begin{cases} \tau = \tau_u = \tau_c > 1 \\ \theta_{\omega=\omega_p} = \arctan(\frac{\tau-\frac{1}{\tau}}{k}) > \theta_{ZVS\min} \\ \frac{\partial P}{\partial \omega} < 0 (\omega_{\infty L} < \omega < \omega_{0H}) \end{cases} \tag{18}$$

where θ_{ZVSmin} is the minimum input impedance angle to achieve ZVS that is related to power devices and drives. The asymmetrical factor is only bounded on one side by (18).

The effect of various asymmetrical factor values on the input impedance angle versus frequency characteristic is shown in Fig. 7 and the frequency has been normalized to frequency that corresponds to the minimum input impedance angle $f_{\theta\min}$, which is equal to f_p in this figure. As illustrated there, near the primary resonant frequency smaller factors lead to smaller variation in input impedance angle. When the input impedance angle variation is small enough, it can be taken to be constant over the target load range near the primary resonant frequency. Asymmetrical factors close to unity enhance insensitivity to load, but operation needs to satisfy (18) and component tolerances need to be considered in a practical design to assure this. Thus, $\tau = 1.05$ has been selected in this design because the value of θ_{ZVSmin} is about 16°.

As mentioned above, design constraints, aiming to achieve ZVS and minimize sensitivity of input impedance angles to coupling and to load, require $\tau > 1$. When, instead, the primary and secondary frequencies match ($\tau_c = 1$) the symmetrical method cannot achieve the same system performance over wide misalignment and load ranges as the proposed method.

B. Design of Coil Inductances and Resonant Circuits

Coil inductances are linked to output power, once the resonant frequencies and switching frequency are chosen. This means that constraints on coil inductances can be obtained from limiting cases on output power when operating at the primary resonant frequency under various coupling conditions.

When the frequency ω_{rated} that corresponds to rated power is near the primary resonant frequency, input impedance angles for frequencies between ω_{rated} and ω_p are nearly constant. Because of these nearly fixed angles, the primary current can be minimized. Variation in input impedance angle and primary current will be minimized over the target coupling range if the output power is below the rated value P_{o} when operating at the primary resonant frequency and the minimum coupling coefficient. The input impedance angle will be approximately constant over the target load range if the output power is less than 50% at the primary resonant frequency and the maximum coupling coefficient. The constraints on mutual inductance can be obtained from these conditions and (4) to give

$$P_o \geq \frac{{U_{CD}}^2\sqrt{\omega^2\frac{{k_{\min}}^2}{\tau^2}-(\omega-\frac{{\omega_p}^2}{\omega})^2}}{L_s[\omega^2{k_{\min}}^2-(\omega-\frac{{\omega_p}^2}{\omega})(\omega-\frac{(\tau\omega_p)^2}{\omega}))]}$$

$$\text{when } \omega=\omega_p \Rightarrow M_{\min} \geq \frac{U_{AB}U_{CD}}{\omega_p P_o}$$

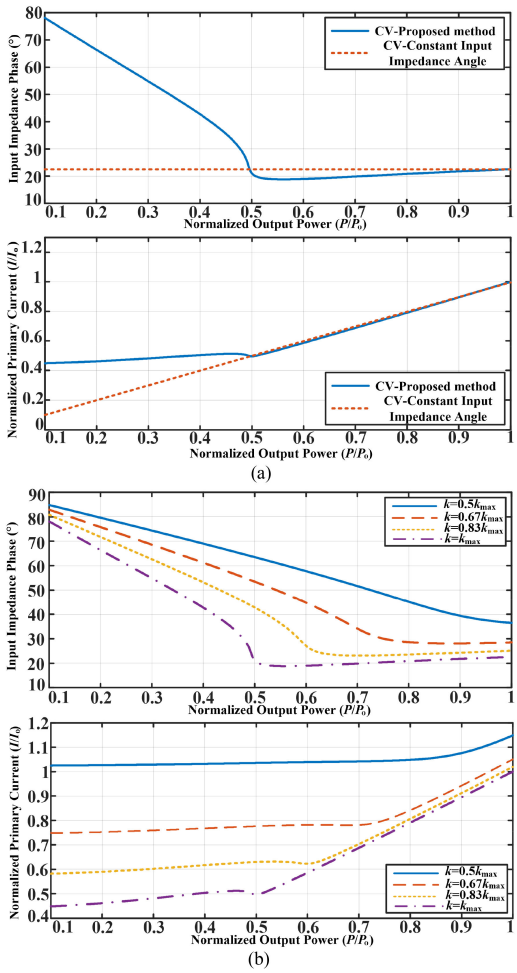

Fig. 9. Input impedance angle and primary current for the proposed method with $\tau = 1.05$ over a 10:1 load power range, and $k_{\max} = 0.31$. (a) Comparisons between the proposed method and constant input impedance angle at $k_{\max}$. (b) Results with the proposed method for various coupling coefficients.

$$0.5P_o \geq \frac{{U_{CD}}^2\sqrt{\omega^2\frac{{k_{\max}}^2}{\tau^2} - \left(\omega - \frac{{\omega_p}^2}{\omega}\right)^2}}{L_s[\omega^2{k_{\max}}^2 - (\omega - \frac{{\omega_p}^2}{\omega})(\omega - \frac{(\tau\omega_p)^2}{\omega})]}$$

$$\text{when } \omega = \omega_p \Rightarrow M_{\max} \geq \frac{2U_{AB}U_{CD}}{\omega_p P_o} \tag{19}$$

where $M_{\min}$ and $M_{\max}$ are the mutual inductance values at the minimum and maximum coupling coefficients, respectively. Combining (2), (3), and (19), coil inductances and compensation capacitances can be obtained. A flowchart of design procedures for the proposed method is given in Fig. 8.

C. System Performance With the Proposed Method

For the IPT system specifications provided in Table I, characteristics of input impedance angle and primary current with the proposed method, given a wide load and misalignment range, are shown in Fig. 9. The input impedance angle with the proposed method, as shown in Fig. 9(a), changes little over the target load range. This can reduce primary current compared to Fig. 3(a). When the output power is less than 50%, the input impedance angle increases, but current is still lower than in Fig. 3(a). As illustrated in Fig. 9(b), input impedance angle increases as coupling coefficient decreases, but the variation in input impedance angle is less than in Fig. 3(b). This means that primary current can be reduced compared to Fig. 3(b). Performance is reduced with misalignment over the target load range, but current is still low. The primary current of the proposed method increases by only 15% over a 2:1 coupling coefficient range with $\tau = 1.05$ at rated load, whereas the primary current increases by more than 100% over this coupling range with a symmetrical method at rated load.

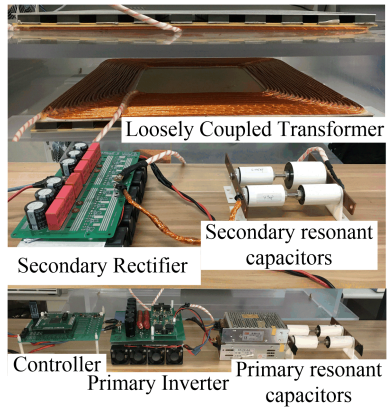

Fig. 10. Experimental platform for the proposed method.

TABLE II
COMPONENT PARAMETERS OF THE PROPOSED IPT SYSTEM

Parameters	Symbols	Measure Values
Dimensions of the loosely coupled transformer	-	600x600 mm
Air gap	-	150 mm
Primary coil inductance	L_p	412.2 μH
Primary coil turns	N_p	22
Secondary coil inductance	L_s	341.9 μH
Secondary coil turns	N_s	21
Primary resonant capacitor	C_p	8.3 nF
Secondary resonant capacitor	C_s	9.0 nF
Switching frequency	f_s	79-103 kHz
Asymmetrical factor	τ	1.05

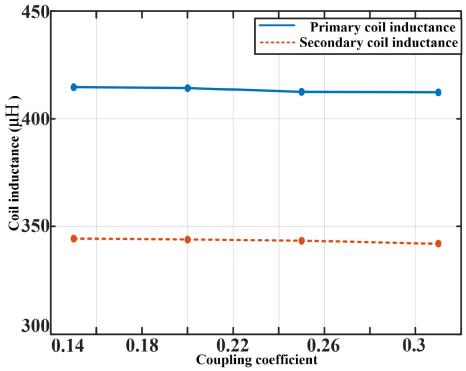

Fig. 11. Coil inductances for the proposed method versus coupling coefficient.

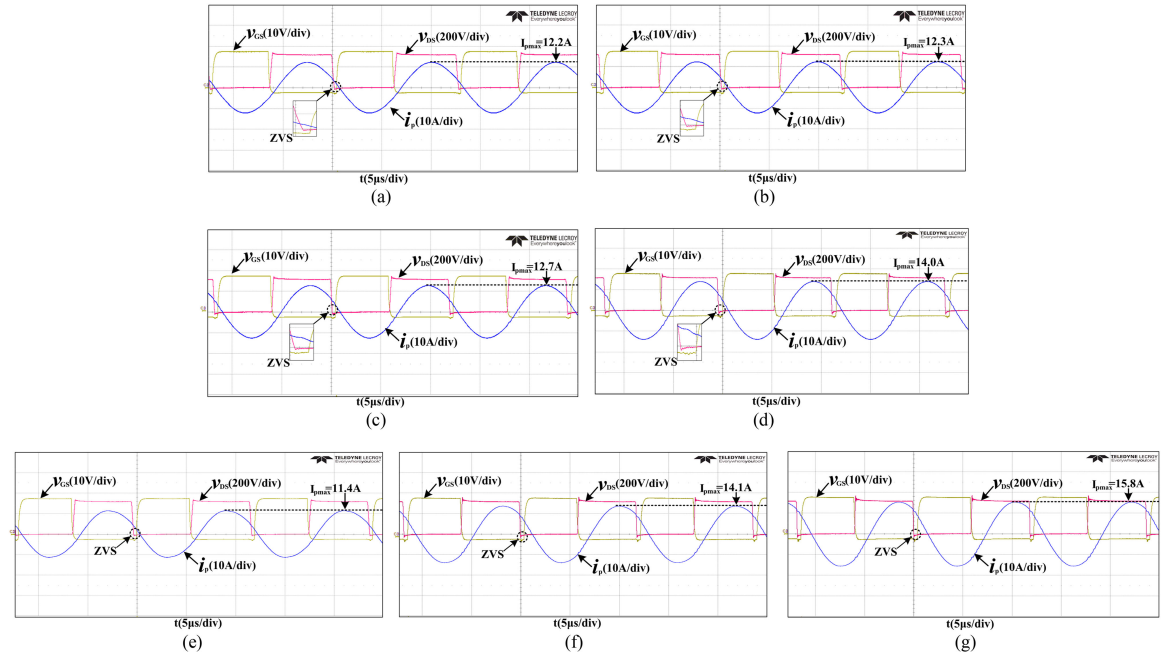

Fig. 12. Comparison between the proposed method and the symmetrical method at rated power and different coupling coefficients: (a) Proposed method at $k = 0.31$. (b) Proposed method at $k = 0.25$. (c) Proposed method at $k = 0.2$. (d) Proposed method at $k = 0.15$. (e) Symmetrical method at $k = 0.31$. (f) Symmetrical method at $k = 0.25$, (g) Symmetrical method at $k = 0.22$.

TABLE III
COMPONENT PARAMETERS OF THE REFERENCE IPT SYSTEM

Parameters	Symbols	Measure Values
Dimensions of the loosely coupled transformer	-	600x600 mm
Air gap	-	150 mm
Primary coil inductance	L_p	350.1 μH
Primary coil turns	N_p	21
Secondary coil inductance	L_s	128.9 μH
Secondary coil turns	N_s	13
Primary resonant capacitor	C_p	11.5 nF
Secondary resonant capacitor	C_s	30.4 nF
Switching frequency	f_s	83-89 kHz

V. EXPERIMENTAL RESULTS

To verify the proposed method, a 2.1-kW prototype IPT system has been prepared, as shown in Fig. 10. The component parameters are given in Table II. Fig. 11 shows how primary and secondary inductances change over the coupling coefficient range of interest. The values change less than 1%, so they can be treated as constant during operation. A separate 2.1 kW prototype that used a symmetrical method was built as a reference for comparison. These two methods were selected to provide the same input impedance angle at rated power and similar switching frequencies. Due to different output power constraints at similar resonant frequencies and switching frequencies, coil inductances and resonant capacitances for circuits that implement the symmetrical method and the proposed method are different [32]. Frequency bifurcation should be avoided for the symmetrical method [33]. Component parameters for the prototype that implements the symmetrical method are given in Table III. Both prototypes use a SiC MOSFET module (SK25MH120TSCp) to form the full-bridge inverter and four ultrafast soft recovery diodes (VS-C4PU6006LHN3) for the rectifier bridge. The system controllers employ a TMS320F28335 processor to generate inverter switching signals. Closed-loop control is implemented by adjusting the inverter switching frequency in real-time to maintain constant output voltage with misalignment over the load range. Load resistances are used to simulate output characteristics.

Fig. 12(a)–(g) shows experimental waveforms that compare the proposed method with the symmetrical method at rated power for various coupling coefficients. Fig. 12(a)–(d) shows results at rated power, with coupling coefficients of 0.31, 0.25, 0.2, and 0.15, respectively. The input impedance angle increases from 21° to 34° – a small range for those cases. The variation in peak primary current is from 12.2 to 14.0 A. This means the current is minimized and high efficiency can be maintained over the target coupling range. Fig. 12(e)–(g) illustrate the symmetrical method at rated power, when the coupling coefficient is 0.31, 0.25, and 0.22, respectively. The primary current will exceed the current rating of the power devices (21 A), when the coupling coefficient is less than 0.22. Compared to the proposed method, the symmetrical method has poor misalignment tolerance for the same device current ratings. The input impedance angle increases from 21° to 46°. The magnitude of primary current rises from 11.4 to 15.8 A for coupling variation from 0.31 to 0.22. Misalignment limits applications of the symmetrical method because current limits will be reached within a lower misalignment range.

Experimental results are shown in Fig. 13(a)–(f) to verify operation of the proposed method compared to the symmetrical method over a wide load range at $k = 0.31$. Fig. 13(a)–(c) shows

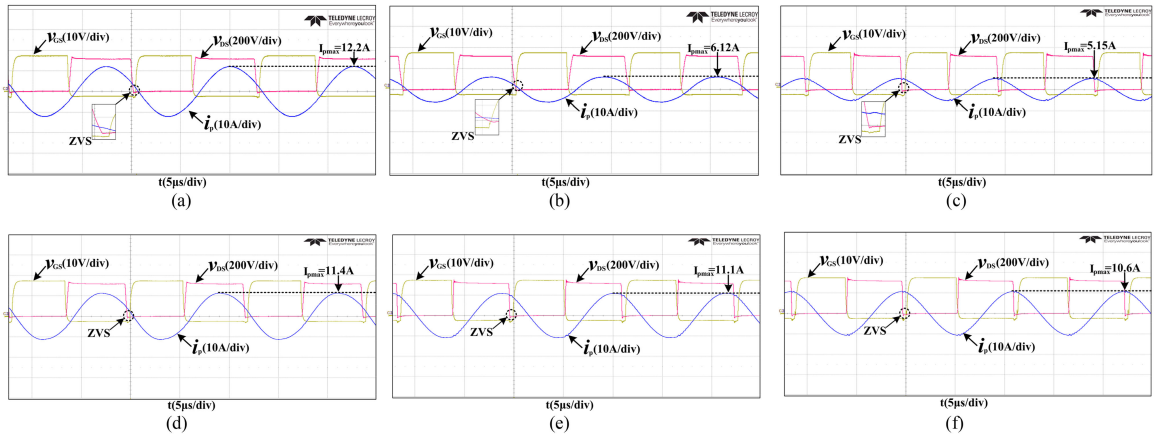

Fig. 13. Comparison between the proposed method and the symmetrical method at $k = 0.31$ and different load resistances. (a) Proposed method at $R_L = 43\ \Omega$. (b) Proposed method at $R_L = 80\ \Omega$. (c) Proposed method at $R_L = 430\ \Omega$. (d) Symmetrical method at $R_L = 43\ \Omega$. (e) Symmetrical method at $R_L = 80\ \Omega$. (f) Symmetrical method at $R_L = 430\ \Omega$.

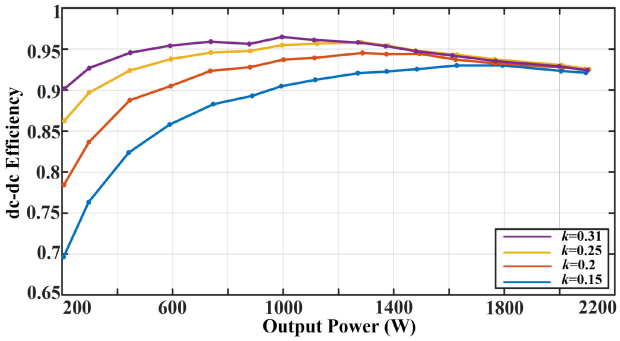

Fig. 14. DC–DC efficiency of the proposed method for various coupling coefficients over a 10:1 load range.

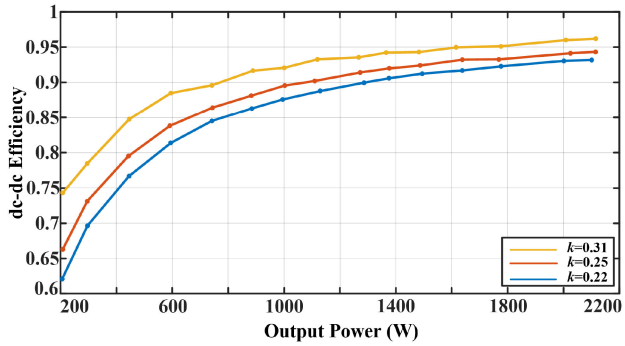

Fig. 15. DC–DC efficiency of the symmetrical method for various coupling coefficients over a 10:1 load range.

experimental waveforms with the proposed method. The input impedance angle varies from 21° to 18° and the primary current falls from 12.2 to 6.12 A from 100% load to 50% load. This supports improved efficiency over the target load range compared to the symmetrical method. When output power decreases from 50% load to 10% load, the input impedance angle increases from 18° to 78°, and the primary current decreases from 6.12 to 5.15 A. Experimental waveforms for the symmetrical method at $k = 0.31$ are shown in Fig. 13(d)–(f), when the load resistance is 43, 80, and 430 Ω, respectively. When the load resistance increases, the input impedance angle increases from 21° to 84° and the primary current decreases from 11.4 to 10.6 A, consistent with the analysis results in Fig. 3(a). Compared to the proposed method, the symmetrical method reduces system efficiency and exhibits high current at light load.

As shown in Fig. 14, the proposed method maintains high efficiency over a 10:1 output power range. For comparison, efficiency of the symmetrical method is shown in Fig. 15, and efficiency decreases substantially as output power decreases. Efficiency with the proposed method is almost constant at rated power regardless of coupling coefficient because the impedance angle and primary current change little within the target coupling range, but efficiency of the symmetrical method reduces with coupling coefficient because the primary current is inversely proportional to coupling coefficient.

The dc–dc efficiency of the proposed method is 92.5% at rated power. The maximum efficiency is 96.5%, achieved at 50% load. Although efficiency within the target load range drops as the coupling coefficient decreases, it is still more than 90% when the coupling coefficient drops in half. Efficiency over a 10:1 load range exceeds 90% at the maximum coupling coefficient.

VI. Conclusion

This article proposes an IPT system based on an asymmetrical factor that seeks to minimize converter and primary resonant circuit currents over a wide misalignment and load range. With this asymmetrical factor, the IPT system can be made to achieve an asymmetrical and monotonic power characteristic, as well as an input impedance angle that is insensitive to coupling and to load, without extra devices and components. The system can maintain ZVS over the allowed range of operating conditions. In the test example, an asymmetrical factor $\tau = 1.05$ led to current increase of only 15% over a 2:1 coupling coefficient variation

range at 100% output power, compared to an increase of 100% for a corresponding conventional symmetrical method.

A 2.1-kW prototype IPT system has been built to demonstrate the feasibility and performance of the proposed approach. At the maximum coupling coefficient, peak efficiency is 96.5%, and efficiency exceeds 90% over the entire allowed load range. Efficiency over the target load range is more than 90% with 2:1 coupling variation.

REFERENCES

[1] J. Huh, S. W. Lee, W. Y. Lee, G. H. Cho, and C. T. Rim, "Narrow-width inductive power transfer system for online electrical vehicles," *IEEE Trans. Power Electron.*, vol. 26, no. 12, pp. 3666–3679, Dec. 2011.

[2] S. Y. Choi, B. W. Gu, S. Y. Jeong, and C. T. Rim, "Advances in wireless power transfer systems for roadway-powered electric vehicles," *IEEE J. Emerg. Sel. Top. Power Electron.*, vol. 3, no. 1, pp. 18–36, Mar. 2015.

[3] G. A. Covic and J. T. Boys, "Modern trends in inductive power transfer for transportation applications," *IEEE J. Emerg. Sel. Top. Power Electron.*, vol. 1, no. 1, pp. 28–41, Mar. 2013.

[4] S. Li and C. C. Mi, "Wireless power transfer for electric vehicle applications," *IEEE J. Emerg. Sel. Top. Power Electron.*, vol. 3, no. 1, pp. 4–17, Mar. 2015.

[5] O. C. Onar, M. Chinthavali, S. Campbell, P. Ning, C. P. White, and J. M. Miller, "A SiC MOSFET based inverter for wireless power transfer applications," in *Proc. IEEE Appl. Power Electron. Conf. Expo.*, 2014, pp. 1690–1696.

[6] W. S. Lee, W. I. Son, K. S. Oh, and J. W. Yu, "Contactless energy transfer systems using antiparallel resonant loops," *IEEE Trans. Ind. Electron.*, vol. 60, no. 1, pp. 350–359, Jan. 2013.

[7] J. Gyu Bum and B. H. Cho, "An energy transmission system for an artificial heart using leakage inductance compensation of transcutaneous transformer," *IEEE Trans. Power Electron.*, vol. 13, no. 6, pp. 1013–1022, Nov. 1998.

[8] Y. Li, J. Hu, F. Chen, S. Liu, Z. Yan, and Z. He, "A new-variable-coil structure-based IPT system with load-independent constant output current or voltage for charging electric bicycles," *IEEE Trans. Power Electron.*, vol. 33, no. 10, pp. 8226–8230, Oct. 2018.

[9] A. Zaheer, M. Neath, H. Z. Z. Beh, and G. A. Covic, "A dynamic EV charging system for slow moving traffic applications," *IEEE Trans. Transp. Electrif.*, vol. 3, no. 2, pp. 354–369, Jun. 2017.

[10] G. Buja, M. Bertoluzzo, and K. N. Mude, "Design and experimentation of WPT charger for electric city car," *IEEE Trans. Ind. Electron.*, vol. 62, no. 12, pp. 7436–7447, Dec. 2015.

[11] S. Ruddell, U. K. Madawala, D. J. Thrimawithana, and M. Neuburger, "A novel wireless converter topology for dynamic EV charging," in *Proc. IEEE Transp. Electrif. Conf. Expo*, 2016, pp. 1–5.

[12] J. H. Kim *et al.*, "Development of 1-MW inductive power transfer system for a high-speed train," *IEEE Trans. Ind. Electron.*, vol. 62, no. 10, pp. 6242–6250, Oct. 2015.

[13] G. Guidi, J. A. Suul, F. Jenset, and I. Sorfonn, "Wireless charging for ships: High-power inductive charging for battery electric and plug-in hybrid vessels," *IEEE Elect. Mag.*, vol. 5, no. 3, pp. 22–32, Sep. 2017.

[14] A. Pevere, R. Petrella, C. C. Mi, and S. Zhou, "Design of a high efficiency 22 kW wireless power transfer system for EVs fast contactless charging stations," in *Proc. IEEE Electr. Veh. Conf.*, 2014, pp. 1–7.

[15] Z. Zhang, H. Pang, A. Georgiadis, and C. Cecati, "Wireless power transfer – an overview," *IEEE Trans. Ind. Electron.*, vol. 66, no. 2, pp. 1044–1058, Feb. 2019.

[16] V. Cirimele, M. Diana, F. Freschi, and M. Mitolo, "Inductive power transfer for automotive applications: State-of-the-art and future trends," *IEEE Trans. Ind. Appl.*, vol. 54, no. 5, pp. 4069–4079, Sep./Oct. 2018.

[17] H. Zeng, S. Vu, Y. Li, and F. Peng, "Design consideration and comparison of wireless power transfer via harmonic current for PHEV and EV wireless charging," *IEEE Trans. Power Electron.*, vol. 32, no. 8, pp. 5943–5952, Aug. 2017.

[18] G. Guidi and J. A. Suul, "Minimizing converter requirements of inductive power transfer systems with constant voltage load and variable coupling conditions," *IEEE Trans. Ind. Electron.*, vol. 63, no. 11, pp. 6835–6844, Nov. 2016.

[19] M. Budhia, G. Covic, and J. Boys, "A new IPT magnetic coupler for electric vehicle charging systems," in *Proc. IEEE Annu. Conf. Ind. Electron. Soc.*, Nov. 2010, pp. 2487–2492.

[20] M. Budhia, J. Boys, G. Covic, and C.-Y. Huang, "Development of a single-sided flux magnetic coupler for electric vehicle IPT charging systems," *IEEE Trans. Ind. Electron.*, vol. 60, no. 1, pp. 318–328, Jan. 2013.

[21] G. A. J. Elliott, S. Raabe, G. A. Covic, and J. T. Boys, "Multiphase pickups for large lateral tolerance contactless power-transfer systems," *IEEE Trans. Ind. Electron.*, vol. 57, no. 5, pp. 1590–1598, May 2010.

[22] A. Zaheer, G. A. Covic, and D. Kacprzak, "A bipolar pad in a 10-kHz 300-W distributed IPT system for AGV applications," *IEEE Trans. Ind. Electron.*, vol. 61, no. 7, pp. 3288–3301, Jul. 2014.

[23] Y. Yao, Y. Wang, X. Liu, Y. Pei, and D. Xu, "A novel unsymmetrical coupling structure based on concentrated magnetic flux for high-misalignment IPT applications," *IEEE Trans. Power Electron.*, vol. 34, no. 4, pp. 3110–3123, Apr. 2019.

[24] R. Mai, B. Yang, Y. Chen, N. Yang, Z. He, and S. Gao, "A misalignment tolerant IPT system with intermediate coils for constant-current-output," *IEEE Trans. Power Electron.*, vol. 34, no. 8, pp. 7151–7155, Aug. 2019.

[25] F. Lu, H. Zhang, H. Hofmann, W. Su, and C. Mi, "A dual-coupled *LCC*-compensated IPT system with a compact magnetic coupler," *IEEE Trans. Power Electron.*, vol. 33, no. 7, pp. 6391–6402, Jul. 2018.

[26] Y. Chen, R. Mai, Y. Zhang, M. Li, and Z. He, "Improving misalignment tolerance for IPT system using a third-coil," *IEEE Trans. Power Electron.*, vol. 34, no. 4, pp. 3009–3013, Apr. 2019.

[27] H. Feng, T. Cai, S. Duan, X. Zhang, H. Hu, and J. Niu, "A dual-side-detuned series–series compensated resonant converter for wide charging region in a wireless power transfer system," *IEEE Trans. Ind. Electron.*, vol. 65, no. 3, pp. 2177–2188, Mar. 2018.

[28] J. Zhao, T. Cai, S. Duan, H. Feng, C. Chen, and X. Zhang, "A general design method of primary compensation network for dynamic WPT system maintaining stable transmission power," *IEEE Trans. Power Electron.*, vol. 31, no. 12, pp. 8343–8358, Dec. 2016.

[29] Y. Chen, B. Yang, Z. H. Kou, Z. He, G. Cao, and R. Mai, "Hybrid and reconfigurable IPT systems with high-misalignment tolerance for constant current and constant voltage battery charging," *IEEE Trans. Power Electron.*, vol. 33, no. 10, pp. 8259–8269, Oct. 2018.

[30] L. Zhao, D. J. Thrimawithana, U. K. Madawala, A. P. Hu, and C. C. Mi, "A misalignment tolerant series-hybrid wireless EV charging system with integrated magnetics," *IEEE Trans. Power Electron.*, vol. 34, no. 2, pp. 1276–1285, Feb. 2019.

[31] E. Gati, G. Kampitsis, and S. Manias, "Variable frequency controller for inductive power transfer in dynamic conditions," *IEEE Trans. Power Electron.*, vol. 32, no. 2, pp. 1684–1696, Feb. 2017.

[32] C. Zheng *et al.*, "High-efficiency contactless power transfer system for electric vehicle battery charging application," *IEEE J. Emerg. Sel. Top. Power Electron.*, vol. 3, no. 1, pp. 65–74, Mar. 2015.

[33] C.-S. Wang, G. A. Covic, and O. H. Stielau, "Power transfer capability and bifurcation phenomena of loosely coupled inductive power transfer systems," *IEEE Trans. Ind. Electron.*, vol. 51, no. 1, pp. 148–157, Feb. 2004.

[34] Q. Chen, S. C. Wong, C. K. Tse, and X. Ruan, "Analysis design and control of a transcutaneous power regulator for artificial hearts," *IEEE Trans. Biomed. Circuits Syst.*, vol. 3, no. 1, pp. 23–31, Feb. 2009.

[35] T. Diekhans and R. W. D. Doncker, "A dual-side controlled inductive power transfer system optimized for large coupling factor variations and partial load," *IEEE Trans. Power Electron.*, vol. 30, no. 11, pp. 6320–6328, Nov. 2015.

[36] T. Diekhans, F. Stewing, G. Engelmann, H. van Hoek, and R. W. De Doncker, "A systematic comparison of hard- and soft-switching topologies for inductive power transfer systems," in *Proc. Elect. Drives Prod. Conf.*, 2014, pp. 1–8.

[37] Z. Zhang, F. Zhu, D. Xu, P. T. Krein, and H. Ma, "An integrated inductive power transfer system design with a variable inductor for misalignment tolerance and battery charging applications," *IEEE Trans. Power Electron.*, vol. 35, no. 11, pp. 11544–11556, Nov. 2020.

[38] Y. Lim, H. Tang, S. Lim, and J. Park, "An adaptive impedance-matching network based on a novel capacitor matrix for wireless power transfer," *IEEE Trans. Power Electron.*, vol. 29, no. 8, pp. 4403–4413, Aug. 2014.

[39] Y. Chen, R. Mai, Y. Zhang, Y. Li, and Z. He, "Inductive power transfer for electric bicycles charging based on variable compensation capacitor," in *Proc. IEEE Appl. Power Electron. Conf. Expo.*, 2017, pp. 1389–1393.

[40] C. S. Wong, Y. P. Chan, L. Cao, L. Wang, K. H. Loo, and M. C. Wong, "A single-stage dynamically-compensated IPT converter with unity-power-factor and constant-output-voltage under varying coupling condition," *IEEE Trans. Power Electron.*, vol. 35, no. 10, pp. 10121–10136, Oct. 2020.

[41] R. Bosshard, J. W. Kolar, J. Muehlethaler, I. Stevanovic, B. Wunsch, and F. Canales, "Modeling and η-α-pareto optimization of inductive power transfer coils for electric vehicles," *IEEE J. Emerg. Select. Top. Power Electron.*, vol. 3, no. 1, pp. 50–64, Mar. 2015.

Zirui Yao (Student Member, IEEE) received the B.S. degree in electrical engineering in 2018 from South China University of Technology, Guangzhou, China, where he is currently working toward the Ph.D. degree in electrical engineering.

His main research interests include inductive power transfer, and resonant converters.

Junjie Zhang received the B.S. degree in electrical engineering from the Huazhong University of Science and Technology, Wuhan, China, in 2019. He is currently working toward the master's degree in electrical engineering with Zhejiang University, Hangzhou, China.

His main research interests include inductive power transfer and capacitive coupled power transfer.

Shiying Luo received the B.S. degree in electrical engineering and automation from Harbin Institute of Technology, Harbin, China, in 2019. He is currently working toward the Ph.D. degree in electrical engineering with Zhejiang University, Hangzhou, China.

His main research interests include inductive power transfer, and resonant converters.

Zhongbao Luo received the B.S. degree in electrical engineering in 2019 from Zhejiang University, Hangzhou, China, where he is currently working toward the master's degree in electrical engineering.

His research interests include wireless power transfer, and resonant converters.

Shaoting Zheng was born in Fujian, China, in 1997. He received the B.S. degree in electrical engineering in 2019 from Zhejiang University, Hangzhou, China, where he is currently working toward the Ph.D. degree in electrical engineering.

His current research interests include wireless power transfer.

Guanxi Li received the B.Sc. degree in electrical engineering in 2016 from Zhejiang University, Hangzhou, China, where he is currently working toward the Ph.D. degree in electrical engineering.

His main research interests include wireless power transfer, including the research of compensation topology and IPT pads.

Zhuhaobo Zhang (Student Member, IEEE) received the B.S. degree in electrical engineering in 2017 from Zhejiang University, Hangzhou, China, where he is currently working toward the Ph.D. degree in electrical engineering.

His main research interests include wireless power transfer, resonant converters, and electric vehicle charging systems.

Philip T. Krein (Fellow, IEEE) received the B.S. degree in electrical engineering and the A.B. degree in economics and business from Lafayette College, Easton, PA, USA, in 1978, and the M.S. and Ph.D. degrees in electrical engineering from the University of Illinois at Urbana–Champaign, Champaign, IL, USA, in 1980 and 1982, respectively

He was an Engineer with Tektronix, Beaverton, OR, USA, and then returned to the University of Illinois at Urbana–Champaign. He was a Senior Fulbright Scholar at the University of Surrey, Guildford, U.K., from 1997 to 1998. From 2003 to 2014, he was a Founder and the Director of SolarBridge Technologies, Inc., Austin, TX, USA, a developer of ac photovoltaic panels. From 2016 to 2020, he was the Executive Dean of the Zhejiang University/University of Illinois at Urbana–Champaign Institute, Haining, China. He was the Grainger Endowed Chair Emeritus in Electric Machinery and Electromechanics, University of Illinois at Urbana–Champaign, where he is the Director of the Grainger Center for Electric Machinery and Electromechanics. He holds 42 U.S. patents. His current research interests include all aspects of power electronics, machines, drives, and electric transportation, with emphasis on nonlinear control approaches.

Dr. Krein was the recipient of the IEEE William E. Newell Power Electronics Award in 2003 and the IEEE Transportation Technologies Award in 2021. He is a the Past President of the IEEE Power Electronics Society, a Past Member of the IEEE Board of Directors, and a Past Chair of the IEEE Transportation Electrification Community. He is an Associate Editor for the IEEE OPEN JOURNAL OF POWER ELECTRONICS. He is a Registered Professional Engineer in Illinois and Oregon. He is a fellow of the U.S. National Academy of Inventors and a member of the U.S. National Academy of Engineering.

Hao Ma (Senior Member, IEEE) received the B.S., M.S., and Ph.D. degrees from Zhejiang University, Hangzhou, China, in 1991, 1994 and 1997, respectively, all in electrical engineering.

Since 1997, he has been a Lecturer, an Associate Professor, and a Professor with Zhejiang University. From 2007 to 2008, he was a Delta Visiting Scholar with the North Carolina State University, Raleigh, NC, USA. He is the Vice Dean of the ZJU-UIUC Institute. He has authored two books and has authored or coauthored over 200 technical papers. His current research interests include advanced control in power electronics, wireless power transfer, fault diagnosis of power electronic circuits and systems, and application of power electronics.

Dr. Ma is currently the Director of Academic Committee of China Power Supply Society. He is an Associate Editor for the IEEE JOURNAL OF EMERGING AND SELECTED TOPICS IN POWER ELECTRONICS and the *Journal of Power Electronics*. He was the AdCom Member of the IEEE Industrial Electronics Society, and the Technical Program Chair of the IEEE ISIE 2012, IEEE PEAC 2014 and IEEE PEAC 2018.